

## FUV Variable Sources in M31

DENIS LEAHY,<sup>1</sup> MEGAN BUICK,<sup>1</sup> JOSEPH POSTMA,<sup>1</sup> AND COLE MORGAN<sup>1</sup>

<sup>1</sup>*Department of Physics and Astronomy, University of Calgary, Calgary, AB T2N 1N4, Canada*

(Received January 1, 2021; Revised January 25, 2021; Accepted March 8, 2021)

Submitted to AJ

### ABSTRACT

The Ultraviolet Imaging Telescope (UVIT) onboard the AstroSat observatory has imaged the Andromeda Galaxy (M31) from 2017 to 2019 in FUV and NUV with the high spatial resolution of  $\simeq 1''$ . The survey covered the large sky area of M31 with a set of observations (Fields) each 28 arcminutes in diameter. Field 1 was observed in two epochs with the F148W filter, separated by  $\simeq 1133$  days ( $\simeq 3.10$  years). The 6.4 kpc diameter Field 1 (at the distance of M31) includes a substantial part of the inner spiral arms of the galaxy. We identify UVIT sources in both epochs of Field 1 and obtain catalogs of sources that are variable in FUV at  $> 3\sigma$  and  $> 5\sigma$  confidence level. The fraction of FUV variable sources is higher for brighter sources, and the fraction is higher in the two main spiral arms compared to other areas. This is evidence that a significant fraction of the FUV variables are associated with hot young stars. Source counterparts are found for 42 of the 86  $> 5\sigma$  FUV variables using existing catalogs. The counterparts include 10 star clusters, 6 HII regions, 5 regular or semiregular variables, 6 other variables and 6 nova or nova candidates. The UVIT FUV-NUV and FUV-FUV color-magnitude diagrams confirm the association of most of the FUV variables with hot young stars. A catalog of UVIT photometry for the variable sources is presented.

*Keywords:* UV astronomy — galaxies:M31 — variability

### 1. INTRODUCTION

The Andromeda Galaxy (M31) is a large spiral with many similarities to our Galaxy and our closest neighboring giant spiral galaxy. It can therefore be used as a template to study parts of our Galaxy that are obscured because of the extinction between our position and theirs. Another advantage to studying objects in M31 is that it has a known distance of  $785 \pm 25$  kpc (McConnachie et al. 2005). As a result, the uncertainty in intrinsic brightness for many objects in M31 is better known than for Galactic sources as most Galactic sources have distance errors greater than those for M31 (3.2%).

At optical wavelengths, M31 has been observed on numerous occasions. The highest resolution observations are from the Hubble Space Telescope, including the Panchromatic Hubble Andromeda Treasury (PHAT) survey

(Williams et al. 2014). In near and far ultraviolet wavelengths (NUV and FUV), the GALEX instrument has surveyed M31 (Martin et al. 2005). Recently M31 has been surveyed in NUV and FUV (Leahy et al. 2020) with the UltraViolet Imaging Telescope (UVIT) on AstroSat.

AstroSat has five instruments. The UltraViolet Imaging Telescope (UVIT) covers the FUV and NUV while the Soft X-ray Telescope (SXT), Large Area Proportional Counters (LAXPC), Cadmium-Zinc-Telluride Imager (CZTI) and Scanning Sky Monitor (SSM) instruments cover soft through hard X-rays (Singh et al. 2014). UVIT observations have high spatial resolution ( $\simeq 1$  arcsec) and the capability to resolve individual stellar clusters and stars in M31. Previous UVIT observations of M31 are presented by Leahy et al. (2020), Leahy & Chen (2020), Leahy et al. (2020b) and Leahy et al. (2018). These papers give a UVIT point source catalog for M31, a match of UVIT sources with Chandra sources in M31, matching UVIT sources with PHAT sources and analysis of UV bright stars in the bulge, respectively.

In this paper, we present results from two epochs of FUV observations in the central 28 arcmin of M31. FUV variable sources are found at significance levels of  $> 3\sigma$  (555 sources) and  $> 5\sigma$  (86 sources). The population frequencies of variable sources are compared for different regions. Color-magnitude diagrams (CMDs) of variable and non-variable sources are compared, indicating that the variable sources are younger and more luminous on average. Counterparts to  $> 5\sigma$  sources are identified by cross-matching with catalogs in the VizieR Web service, and their nature further investigated by NUV and FUV CMDs. The Appendix describes data processing that improves the photometric accuracy for moderately crowded regions.

## 2. OBSERVATIONS AND DATA ANALYSIS

M31 was observed in FUV and NUV at  $\sim 1''$  spatial resolution by UVIT (Leahy et al. 2020). It was covered in nineteen 28 arcmin diameter fields (Fig. 2 of Leahy et al. 2020).

UVIT Field 1 was observed in the F148W, F172M, N219M and N279N filters near the beginning of the observing project and in a new observation that has not been reported previously. The first observation is referred to as Observation A, the second as Observation B. Observation B was made in filters F148W, F169M and F172M. The F172M filter is narrow with  $\delta\lambda = 12.5$  nm vs. 50 nm for F148W (Tandon et al. 2017), thus has lower S/N than images in F148W. F148W is used for the variability search because it gives high S/N. Only a fraction of the variables show up as variable above the  $3\sigma$  level in F172M, and all of those are detected variables in F148W. Thus we detect variable sources by analysis of the F148W data.

The field centers, filters, exposure times and dates of the observations for Field 1 are shown in Table 1. The basic data processing was carried out using updated data processing and calibration methods (Leahy et al. 2020), including new astrometry corrections (Postma & Leahy 2020).

### 2.1. Source Finding

Because of the satellite pointing drift of AstroSat, the edges of the UVIT field of view have low exposure time and high noise level. Thus we avoid the outer edge for source finding. We measured a position along a line NW from the centre in the exposure map where it has a value of 10% for observation A. Then we took one position 0.5 arcmin closer to the center of the image and measured an exposure of  $\simeq 70\%$ , and a second position another 0.5 arcmin closer to the center, where we measured an exposure of  $\simeq 95\%$ . Nearly the same values were obtained

from measurements of the exposure image for observation B. Our search for sources was restricted to areas with exposure values  $\gtrsim 50\%$  in both images. Thus we avoid areas that are within  $\sim 1$  armin of the edge of either image for source finding. Figure 1 shows the exposure maps for Observations A and B and the non-variable<sup>1</sup> sources detected in both images. This illustrates the different pointing centers of the two observations and the choice of sky area used for source finding in both images.

Because of the bright diffuse FUV emission from the bulge, the source finding methods (Postma & Leahy 2017, Postma & Leahy 2020, Postma & Leahy, 2021 accepted for J. Astrophys. Astr.), did not produce reliable results in a region of  $\simeq 2$  armin radius centered on the bulge. In future work, we plan to develop a source finding method for UVIT data that works reliably in regions of bright diffuse emission. Thus, a circular area with radius 300 pixels<sup>2</sup> (2.1 arcmin) centered on the bulge was removed for the current analysis. The center of the bulge is offset west of center in the images: the omitted region is visible in Figure 1.

Source locations were found in observations A and B in the F148W filter. We used a threshold peak pixel signal to noise ratio (SN) of 3 for A and 4.5 for B and a threshold integrated SN<sup>3</sup> of 30 for A and 45 for B. The higher SN level for observation B was chosen to approximately match the sensitivity levels because observation B had  $\sim 3$  times the exposure time<sup>4</sup>.

### 2.2. Source Magnitude Extraction

The UVIT photometry is calibrated with respect to a Curve of Growth (COG) extracted with radius 95 pixels (40'') (Tandon et al. 2020). This method is not applicable in practice when sources are separated by less than 40'': an alternate extraction method is necessary. For the UVIT images of M31, with their large number of sources, testing revealed that fitting pixels in a 9x9 box gave good results and minimal interference by neighboring sources for the majority of sources.

Because of various factors, including residual errors in the calibration of the optics and detector non-

<sup>1</sup> The variable sources are a small fraction of all sources so inclusion of both sets does not significantly change the delineation of the edge of the areas studied.

<sup>2</sup> The UVIT pixels are  $0.4168''$  by  $0.4168''$ .

<sup>3</sup> This is the minimum ratio of (detected counts above background summed over pixels in the detection window) to (background counts summed over pixels in the window).

<sup>4</sup> Other methods were used for finding sources in A and B down to the same sensitivity limit. This included source finding on the image produced by merging data from observations A and B, which was unsuccessful due to the different exposure times of the two images. The chosen method produced the best results.

**Table 1.** M31 UVIT Observations for UVIT field 1.

Observation	RA(deg) <sup>a</sup>	Dec(deg) <sup>a</sup>	Filter <sup>b</sup>	Exposure Time	Mean BJD <sup>c</sup>
A	10.71071	41.25023	a, c, d, e	7872, 3875, 7920, 4347	2457671 (+0.8010,+1.2626,+0.8010,+1.2626)
B	10.71071	41.25023	a, b, c	17191, 10427, 18177	2458804 (+1.3243,+0.8591,+2.2231)

NOTE—a. RA and Dec are the J2000 coordinates of the nominal pointing center of the observation.

b. Filter labels are a: F148W, b: F169M, c: F172M, d: N219M, e: N279N.

c. Mean BJD is the mean solar-system Barycentric Julian Date of the observation. The common integer part for multiple observations is given as the first number.

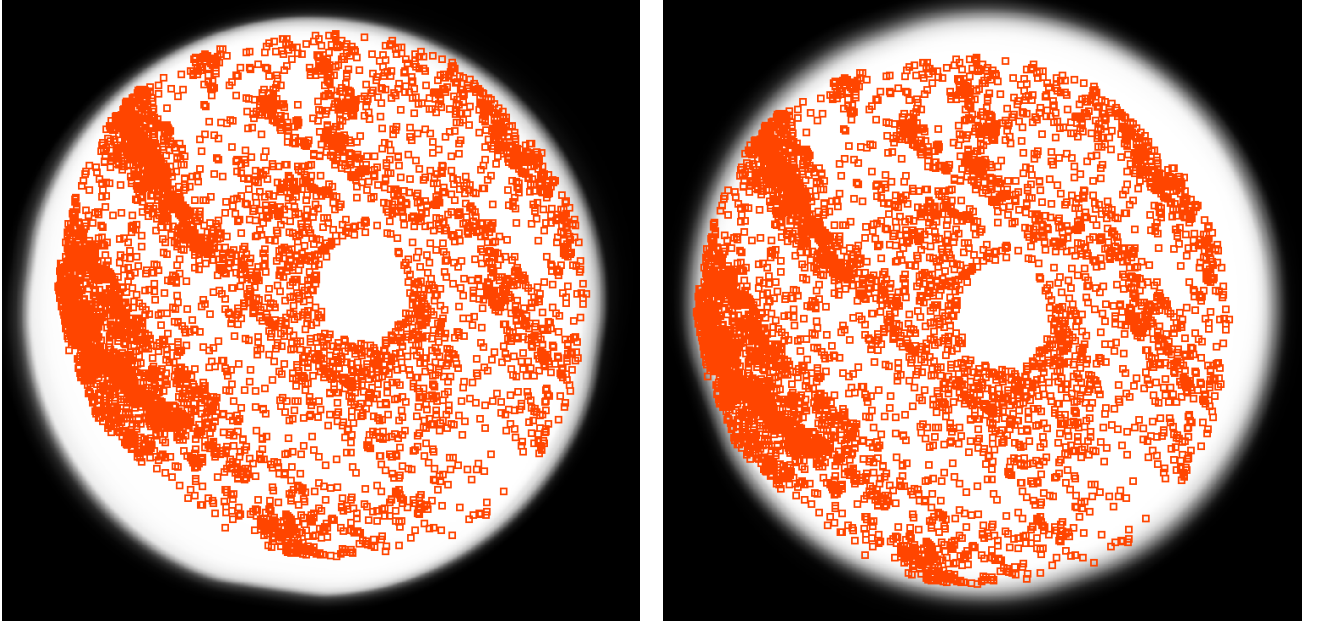


**Figure 1.** Field 1 F148W exposure maps for Observation A (left panel) and Observation B (right panel). The greyscale at bottom goes from black (0% of exposure time) to white (100% of exposure time). The center of Observation B is shifted by  $\simeq 2.2$  arcminutes NW of the center of Observation A. The red squares mark the locations of the sources detected as non-variable in both images.

uniformities and satellite pointing drift corrections (which are different for each observation), each source in the image has a slightly different PSF. There are also variations in the detected image for each source from photon counting statistics. Thus unique point-spread function (PSF) fits are required to each source. We have tested extensively that sources are fit well and consistently by using an elliptical Gaussian with variable parameters.

The count rates from elliptical Gaussian fits were corrected for the UVIT point-spread-function as described in Appendix A. They were then converted to AB magnitudes using the calibration determined in [Tandon et al. \(2020\)](#). We describe the details of this process in Appendix A, including a correction to match UVIT N279N magnitudes to HST/PHAT ([Williams et al. 2014](#)) F275W magnitudes.

A source match was performed on the F148W filter source lists from observations A and B using the TopCat catalog software ([Taylor 2005](#)). Overall, 3164 sources were found in both observations A and B. Upon removing the matched sources from each the source lists from observation A and B, we found 1383 sources in A that are not detected in B (‘AnotB’ sources), and 1431 sources in B that are not detected in A (‘BnotA’ sources). These latter two source lists were used to determine upper limits of ‘AnotB’ sources for Observation B, and upper limits in ‘BnotA’ sources for Observation A. The upper limits were found by carrying out forced photometry at the known source positions, i.e. elliptical Gaussian fits with normalization (source flux in counts/s) as the only free parameter. The upper limit was taken as the fit flux (or zero if the fit flux was negative) plus its uncertainty. The total number of distinct

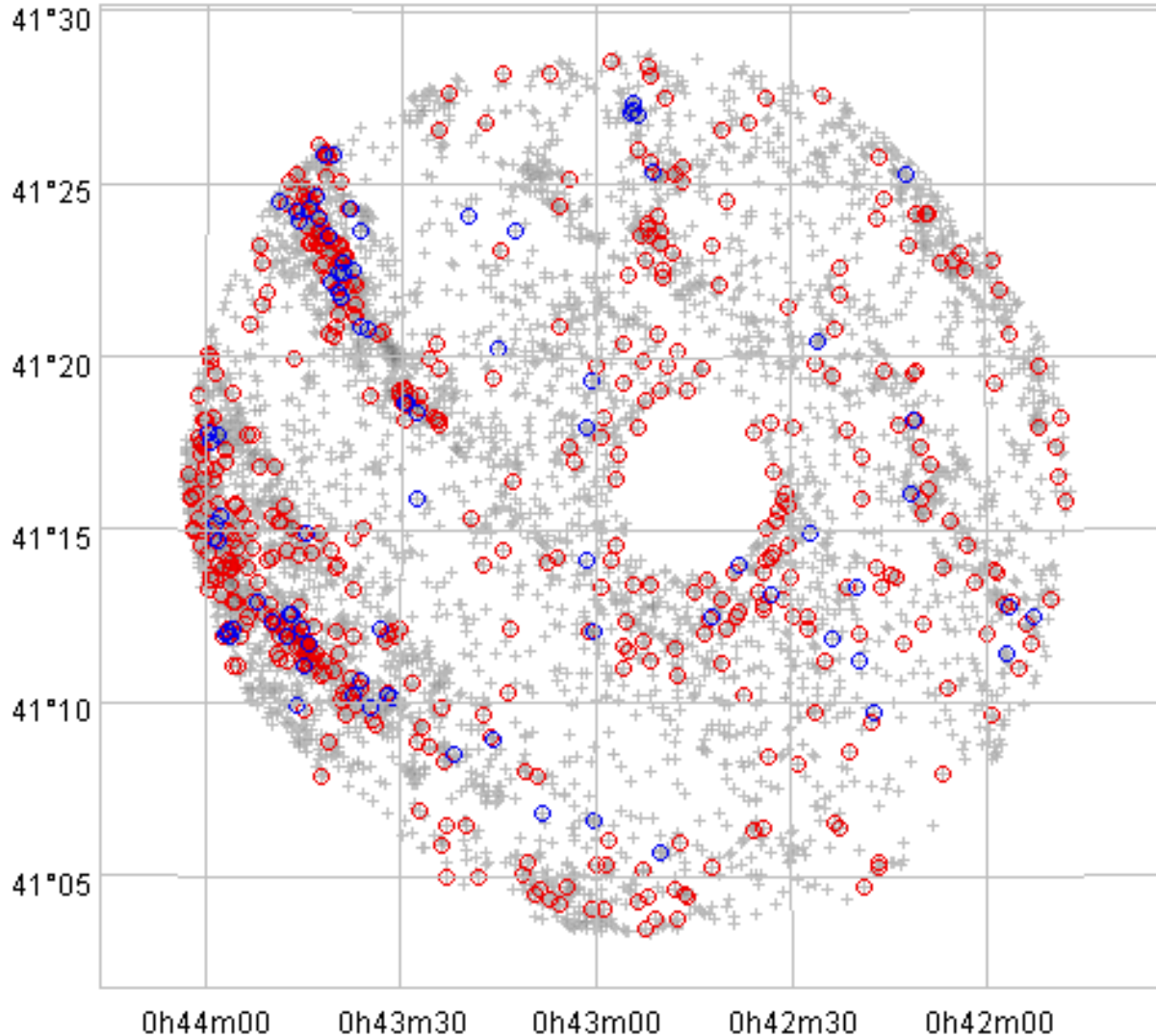


**Figure 2.** Field 1 with all identified UVIT sources from observations A and B (grey crosses),  $> 3\sigma$  variable sources (red circles) and  $> 5\sigma$  variable sources (blue circles). The central part of the bulge is visible as the blank area right of center.

sources detected in either A or B is 5970. The positions of the sources are shown in Figure 1.

Using this list of F148W source positions, we carried out source finding on the N279N and N219M images from Observation A, and on the F172M and F169M images from Observation B. If the nearest light maxima in any of these filters was inconsistent with the F148W position (more than  $1''$  away), we list the filter magnitude as no detection. This yields UVIT multiband magnitudes for most of the sources.

### 2.3. Identification of Variable Sources

The result of the source finding and fitting was F148W magnitudes or upper limits for a total of 5970 different sources. Requiring that the difference in magnitudes between observations A and B is  $> 3$  times the combined uncertainty of A and B magnitudes (labelled  $\sigma$  here) in

the measurements, the number of  $> 3\sigma$  variable sources is 555. 86 of these sources are variable at the  $> 5\sigma$  level<sup>5</sup>. The positions of the  $> 3\sigma$  variable sources and  $> 5\sigma$  variable sources are shown in Figure 2.

We checked that the variable sources are not detected preferentially near the field edges (see Fig. 1 for the field edges seen in the exposure maps for Observations A and B). The radial distribution of source numbers vs. distance from the mean field center (average of field centers of Observations A and B) is shown in Figure 3. The numbers of non-variable sources per bin are multiplied

<sup>5</sup> Using the source finding and fitting routines we originally detected 94  $> 5\sigma$  variables. We manually inspected each fit and found 86 were good fits (true variables), 3 were bad fits to non-variable sources and 5 were blended/crowded sources that could not be fit, resulting in 86 verified  $> 5\sigma$  variables.

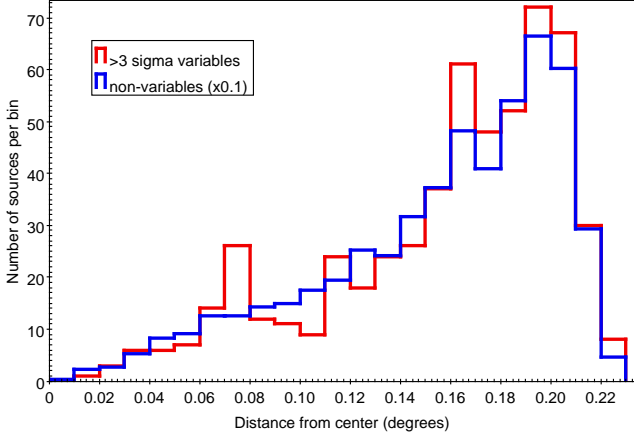


**Figure 3.** Distributions of variable and of non-variable sources vs. distance from the field center.

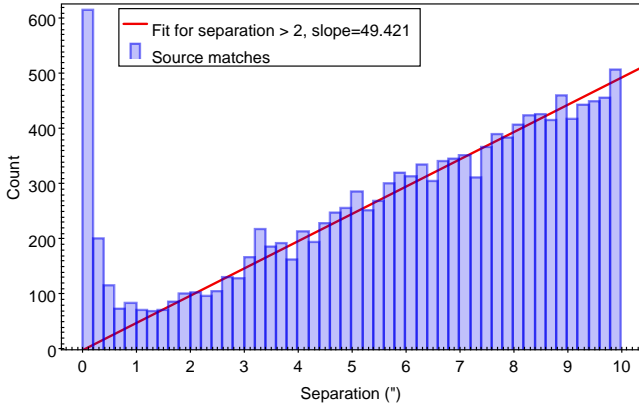


**Figure 4.** Number of matches between sources in the UVIT Region 1 F148W at different separations. The line shows the best fit line to separations greater than 2", which give the expected number of accidental matches.

by a factor of 0.1 so that the distribution of variables and non-variables can be compared easily. It is seen that they agree on the large scale, within Poisson counting errors, with no peak at the field edge. It is noted that the field edge here is outside the largest bin plotted because we only carried out source finding for  $\gtrsim 1$  arcmin from the field edges.

#### 2.4. Positional Errors for UVIT Sources

The UVIT F148W source positions were checked against the source positions in PHAT (Williams et al. 2014) and against source positions in Gaia DR2 (Gaia Collaboration et al. 2018, Gaia Collaboration et al. 2016). The complete source list from the combined observation A and B measurements was matched to the PHAT F275W filter catalog for sources in PHAT brighter than Vega magnitude 21 within a search radius of 1", yielding 1571 matches. From these sources, the mean difference (PHAT-UVIT position) in RA is 0.128" with a standard deviation of 0.238". In DEC, the mean difference (PHAT-UVIT position) is 0.0068" and the standard deviation is 0.158".

The source list from the combined observation A and B measurements was matched to the Gaia DR2 positions with search radius of 1", yielding 974 matches. The mean difference in RA (Gaia-UVIT position) was 0.038" with a standard deviation of 0.322". The mean difference in DEC (Gaia-UVIT position) was 0.014" with a standard deviation of 0.221". We use the Gaia DR2 offsets as the best estimate of the mean UVIT position offset and scatter. Both are significantly smaller than the UVIT spatial resolution of 1", indicating that our astrometry calibration worked well.

**Table 2.** Photometry<sup>a</sup> for  $> 3\sigma$  variable FUV sources measured in UVIT Field 1.

UVIT	UVIT	F148W_A	F148W_B	F148W_A	F148W_B	F148W	N279N_A	N279N_A	N219M_A	N219M_A	F172M_B	F172M_B	F169M_B	F169M_B
RA <sup>b</sup>	DEC <sup>b</sup>	mag	err	mag	err	Sigma	mag	err	mag	err	mag	err	mag	err
10.487075	41.190926	20.44	0.08	24.79	0.24	20.8	18.75	0.07	22.38	0.23	.	.	.	.
10.925487	41.431048	20.09	0.08	22.12	0.1	18.06	.	.	.	.	19.76	0.06	19.78	0.05
10.723582	41.449845	20.11	0.08	18.9	0.07	17.55	20.56	0.15	.	.	.	.	.	.
10.992857	41.29603	21.92	0.12	19.78	0.07	16.95	19.48	0.09	19.5	0.07	19.37	0.05	19.55	0.05
10.57196	41.162304	21.18	0.1	99.99	99.99	15.49	18.53	0.06	19.49	0.07	.	.	.	.
10.922499	41.392021	22	0.12	20.13	0.08	13.63	20.12	0.13	19.65	0.07	19.73	0.06	19.97	0.05
10.895092	41.165119	19.06	0.07	18.45	0.07	13.23	18.63	0.07	18.89	0.06	18.71	0.05	18.98	0.04
10.723116	41.449416	19.88	0.08	19.04	0.07	12.91	.	.	.	.	21.13	0.11	22.19	0.13
10.756415	41.299913	24.65	0.33	20.81	0.08	12.23	12.23	.	.	.	19.9	0.07	20.39	0.06
10.880259	41.169574	21.94	0.12	20.29	0.08	12.07	20.18	0.13	20.28	0.09	19.93	0.07	20.29	0.06

NOTE—a: Magnitudes are in the AB system; the value . indicates no detection. b: RA and DEC are measured in degrees.

NOTE—Table 1 is published in its entirety in the machine-readable format. A portion is shown here for guidance regarding its form and content.



The observed density of detected UVIT sources determines the number of accidental matches we can expect caused by source crowding. The combined UVIT observation A and B F148W sources were internally cross-matched up to a radius of  $10''$ , keeping all matches for each source. The resulting distribution of numbers of sources vs. separation is shown in Figure 4. The sharp peak centered on  $0''$  separation indicates the real matches. Fitting the numbers with separations greater than  $2''$  with a linear regression line gave a slope of 49.4 counts/bin/ $''$  (using bins of  $0.2''$ ).

To estimate the contamination of accidental matches, we integrated the corresponding area under the line for sources between  $0''$  and  $1''$  to get 123. The number below the line for sources between  $1''$  and  $2''$  is 371. To estimate the number of real matches we sum the actual sources above the line to get: 593 between  $0''$  and  $1''$  and 29 between  $1''$  and  $2''$ . This means we are getting approximately 123 accidental matches between  $0''$  and  $1''$  (about 17% of the matches in  $0-1''$ ), and we are missing about 29 real matches between  $1''$  and  $2''$  (about 7% of the matches in  $1-2''$ ) by choosing a  $1''$  upper limit for UVIT matches. If we chose a smaller cutoff, we could reduce the accidentals at the expense of losing more real sources, but we take  $1''$  as a realistic compromise.

### 3. RESULTS AND DISCUSSION

#### 3.1. Catalog of FUV Variables

For observation A, the UVIT filters were F148W, N219M and N279N, allowing multiband photometry for the sources detected in the F148W filter. Similarly for observation B, the UVIT filters were F148W, F169M and F172M. From this set of photometry, we created a catalog of the  $> 3\sigma$  variables, which includes the  $> 5\sigma$  variables. This catalog is presented here (first 10 entries) by Table 2, and in full as an online machine readable table.

#### 3.2. Quantifying the Variability

The magnitude differences between the two observations, separated by  $\sim 3.1$  years, were found for the set of 3 to  $5\sigma$  variables and for the set of  $> 5\sigma$  variables. Figure 5 shows the histograms of magnitude differences for both sets. The mean magnitude differences translate to a mean flux ratio of 3.1 for the 3 to  $5\sigma$  variables, and a mean flux ratio of 3.8 for the  $> 5\sigma$  variables. As seen in Figure 5, the drop in number of sources for magnitude differences  $\lesssim 0.75$  for 3 to  $5\sigma$  variables, and for  $\lesssim 0.25$  for  $> 5\sigma$  variables can be explained by the typical magnitude errors in the UVIT measurements ( $\simeq 0.06$  at

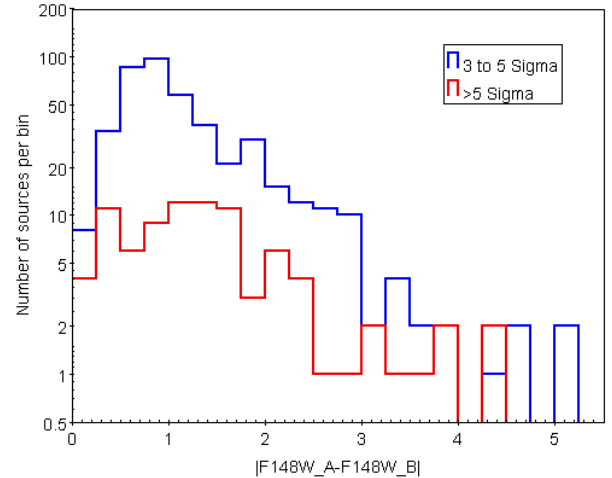


**Figure 5.** Histogram of F148W magnitude differences, for  $> 5\sigma$  set and 3 to  $5\sigma$  set (log scale on vertical axis). The mean magnitude difference for the  $> 5\sigma$  set is 1.45, for the 3 to  $5\sigma$  set is 1.23.

F148W magnitude 17, increasing smoothly to  $\simeq 0.2$  at magnitude 23).

The distribution of magnitudes from observation A for the variable and non-variable sources is shown in the left panel of Figure 6. The majority of sources are non-variable ( $< 3\sigma$ ), with the turnover at F148W magnitude of  $\simeq 23.4$  representing the approximate sensitivity limit of UVIT F148W detection, for an observation time of 8000s. The turnovers in the distributions of 3 to  $5\sigma$  variables and  $> 5\sigma$  variables are at  $\simeq 23$  and  $\simeq 22.6$ , respectively. These are consistent with observational limits determined by magnitude errors. Above these limits, the shape of the magnitude distribution should reflect the intrinsic distribution of source numbers. Of interest is the fraction of variable sources as a function of magnitude. This is illustrated in right panel Figure 6. The error bars are calculated using counting errors and increase for bright sources because of the few sources in the brighter magnitude bins. The decrease in fraction of variables for faint sources ( $\gtrsim 22$ ) is due to observational limits. The increase in fraction of variables for bright sources should be intrinsic. The variable fraction for 3 to  $5\sigma$  variables is  $\sim 15\%$ , and is consistent with no change as a function of magnitude. For the  $> 5\sigma$  variables, the fraction of variable sources shows weak evidence for an increase with increasing brightness.

#### 3.3. Spatial Distribution of the Variables

A visual comparison of all UVIT sources with the  $> 3\sigma$  variable sources in Figure 2 shows that the variable sources appear to be concentrated in the two main spiral arms in the southeast and northeast parts of the image. To test this, we used the polygon feature in TopCat

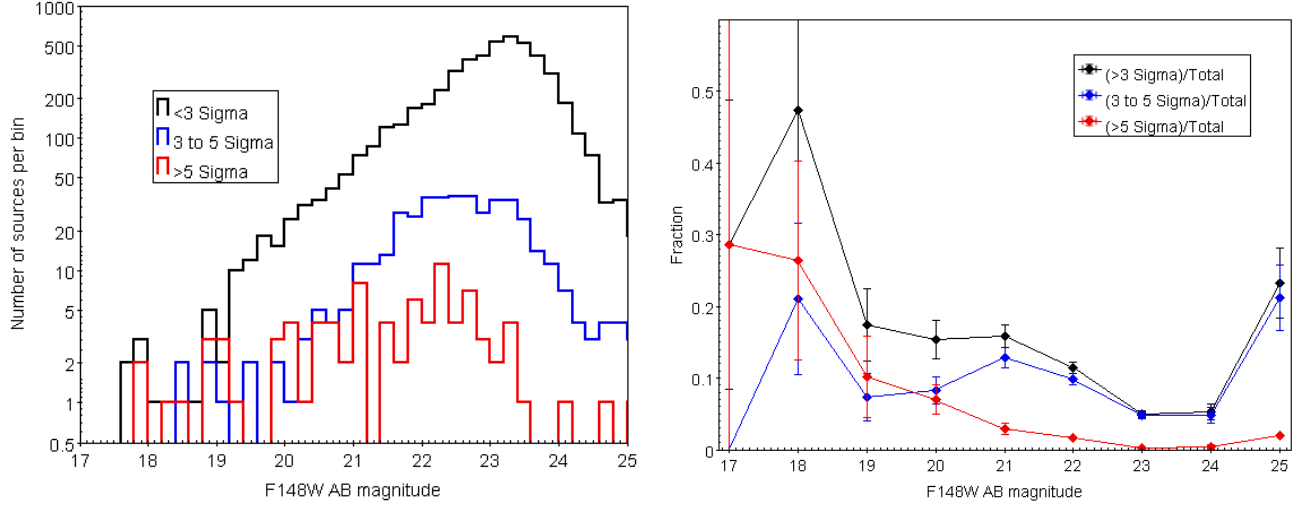


**Figure 6.** Left panel: Histogram of magnitudes for variable and non-variable sources, using F148W magnitudes from Observation A. Right panel: Fraction of variables in different categories to total number of sources, in 1 magnitude wide bins.

**Table 3.** Numbers of sources,  $> 3\sigma$  variables and  $> 5\sigma$  variables in different areas, and their ratios.

	SEarm	NEarm	NotSE,NE <sup>1</sup>	Ext. <sup>1</sup> SEarm	Ext. <sup>1</sup> NEarm	Ext. <sup>1</sup> NWarm	interarm <sup>1</sup>
total number	938	1704	3330	1364	538	768	660
$> 3\sigma$ var.	101	187	268	118	50	48	52
$> 5\sigma$ var.	23	30	35	15	5	8	7
$> 3\sigma$ var./total	$0.108 \pm 0.011$	$0.110 \pm 0.008$	$0.081 \pm 0.005$	$0.087 \pm 0.008$	$0.093 \pm 0.014$	$0.063 \pm 0.009$	$0.079 \pm 0.011$
$> 5\sigma$ var./total	$0.025 \pm 0.005$	$0.018 \pm 0.003$	$0.011 \pm 0.002$	$0.011 \pm 0.003$	$0.09 \pm 0.004$	$0.010 \pm 0.004$	$0.011 \pm 0.004$

NOTE—1. NotSE,NE stands for everything but the areas covered by SEarm and NEarm; Ext. stands for Extended, and does not include the SEarm or NEarm areas; the interarm area shown by the grey symbols in Figure 5.

to select a number of different groups of sources. The seven groups consisted of one group each for the dense part of the southeast and northeast spiral arms (SEarm and NEarm); a group in the extended part of the southeast arm (Ext.SEarm); a group in the extended part of the northeast arm (Ext.NEarm); a group in the extended part of the northwest arm (Ext.SWarm); a group of sources including all other sources except those in the southeast and northeast spiral arms (notSE,NE); and a group for interarm sources (not in either the dense parts of the arms or the extended parts of the arms: notSE,NE, notExt.SE,NE,SW). These first 5 of these groups are shown by the color-coded symbols in Figure 7 and the last group shown by the grey symbols.

Table 3 shows the results from counting sources in the different groups with Poisson errors. The results show the SEarm and NEarm have the same fraction of  $> 3\sigma$  variables within errors. The area notSE,NE has a lower fraction of  $> 3\sigma$  variables compared to the NEarm, with  $3\sigma$  confidence. A comparison of the Ext.SE, Ext.NE and Ext.NW arms shows that the fraction of  $> 3\sigma$  variables is consistent between the Ext.SE and Ext.NE areas, but higher than the Ext.NW area by  $2\sigma$  confidence.

The difference between the fraction of  $> 3\sigma$  variables in Ext.SEarm or Ext.NEarm and the interarm area is only  $\sim 1\sigma$  confidence.

For the  $5\sigma$  variables, the SEarm has a higher fraction of variables than the NEarm by  $1.2\sigma$  confidence, and higher by  $2.6\sigma$  confidence than for the NotSE,NE area. The extended arm areas and the interarm area are consistent with each other in fraction of variables. In summary, we find that the dense arms (SEarm, NEarm) have a significantly larger fraction of variables than the rest of the field, considering both  $> 3\sigma$  and  $> 5\sigma$  variables. However there is no significant difference between the extended arms and the interarm area.

The UVIT F148W filter (150 nm band) is sensitive to detection of hot luminous stars. The above results imply that the fraction of variable sources is significantly higher in the regions with the highest hot star density compared to either the regions with lowest density or medium density. The regions with the lowest density and with a medium density of hot stars have indistinguishable fractions of variable stars. In particular the high density SEarm and NEarm have higher fraction of variables by a factor of  $\sim 1.4$  (from the  $> 3\sigma$  variables



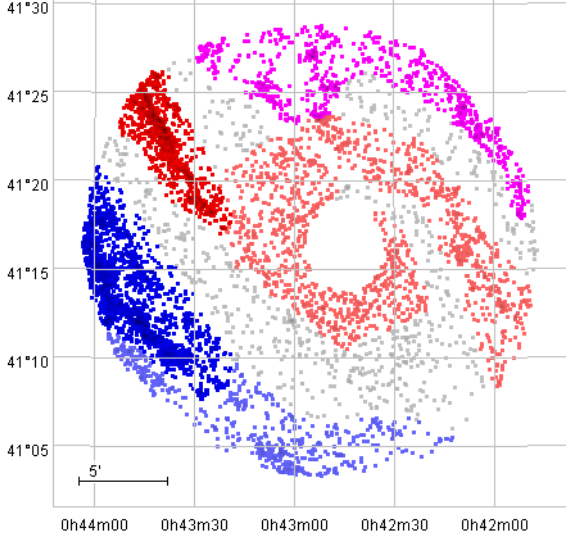


**Figure 7.** Areas used for spatial analysis of variable sources. All UVIT variable and non-variable sources from observations A and B are shown by the squares (grey and colored); The sources in the dense part of the southeast arm (‘SEarm’) are shown in blue; those in the dense part of the northeast spiral arm (‘NEarm’) in red; those in the extended part of the southeast arm (‘Ext.SEarm’) by light blue; those in the extended part of the northeast arm (‘Ext.NEarm’) by pink; those in the extended part of the northwest arm (‘Ext.NWarm’) by magenta; and those not in either the dense or extended parts of the arms (‘interarm’) by grey. The central part of the bulge is visible as the blank area left of center.

in Table 3) to  $\sim 2$  (from the  $> 5\sigma$  variables) compared to the other 5 areas listed in the Table.

### 3.4. Colour Magnitude Diagrams

From the photometry for the variable sources and the photometry for the non-variable sources ( $< 3\sigma$  difference in F148W magnitudes between Observation A and Observation B), we construct FUV-NUV CMDs. For Observation A, we use FUV-NUV color and NUV AB magnitude, with NUV chosen as either N279N or N219M, for the three sets: all detected sources;  $3-5\sigma$  variables; and  $> 5\sigma$  variables. The N279N vs. F148W-N279N CMD is shown in Figure 8. The N219M vs. F148W-N219M CMD looks similar. For Observation B, there were three FUV filters, allowing construction of CMDs using FUV 2-color and FUV AB magnitude, for the same three groups of sources. The F172M vs. F148W-F172M CMD is shown in Figure 9. The F169M vs. F148W-F169M CMD looks similar.

On the CMDs, we plot isochrones from the CMD web isochrone generator at <http://stev.oapd.inaf.it/cmd>. These isochrones use solar metallicity, the foreground extinction to M31 of  $A_V=0.2$  and other parameters set to default in the isochrone generator. We also calculated

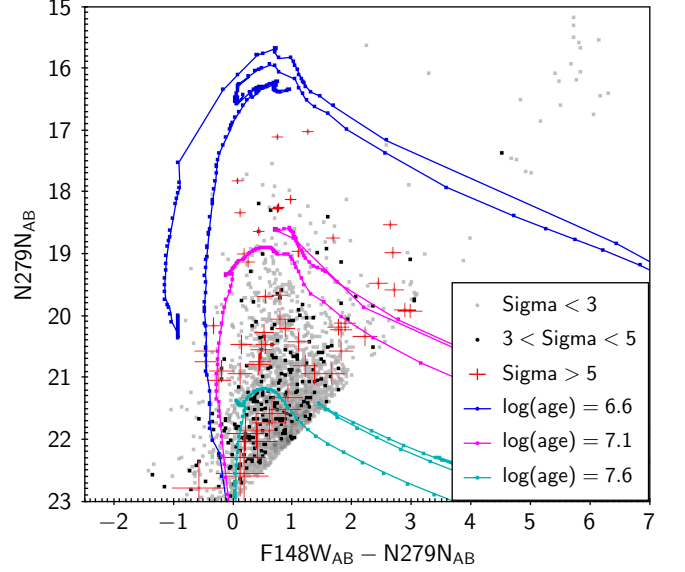


**Figure 8.** Field 1 Observation A colour magnitude diagram (CMD): N279N versus F148W-N279N. The gray points are all detected sources in Observation A, the black points are the  $> 3\sigma$  variables, and the red points with error bars are the  $> 5\sigma$  variables. The error bars for the gray and black points are similar in size, but not shown to avoid crowding. Isochrones are from the CMD web isochrone generator at <http://stev.oapd.inaf.it/cmd>, and are plotted as the points joined by solid lines, with  $\log(\text{age})$  values of 6.6 (blue lines), 7.1 (magenta lines) and 7.6 (cyan lines).

isochrones for metallicity of  $\log(Z/Z_\odot)=-1$  and  $-2$  but this did not result in a large shift of the isochrones (comparable to the size of the data error bars). Increased extinction moves the isochrones almost vertically downwards (increase in magnitude but little change in color).

From Figures 8 and 9, the majority of the data points are consistent with stars aged  $\sim 5 \times 10^6$  yr to  $\sim 1 \times 10^8$  yr. These are young stars. The UVIT observations select stars which are brightest in FUV and NUV bands, so we expect a strong selection for the youngest stars in M31. A small fraction of the data points lie at the upper right in the diagram, away from where the model isochrones lie. These points are probably cool foreground stars in the Milky Way. If those stars were at the distance of M31 they would be shifted down by the difference in distance modulus (e.g., by 14.46 magnitudes if the foreground stars are at 1 kpc). This would move them into the region consistent with isochrones with ages of a few Gyr (at N279N magnitude of  $\sim 30$ ).

### 3.5. Source Matching to Counterparts at Other Wavelengths

For the set of 86  $> 5\sigma$  variable sources, a search was performed for previously detected objects. The

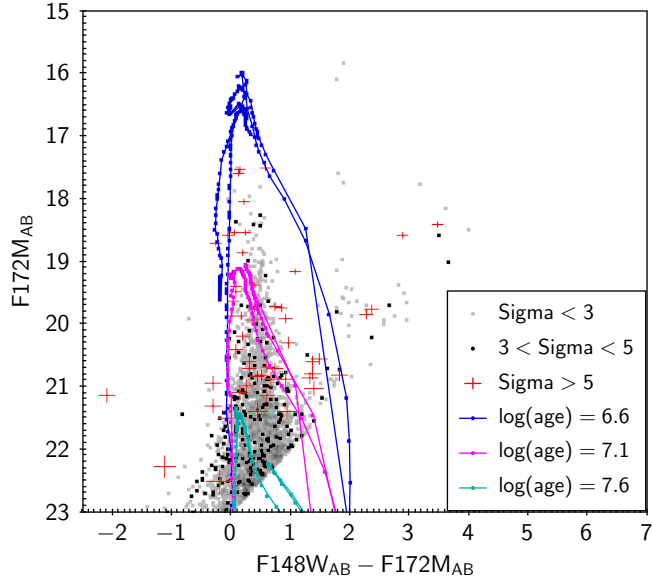


**Figure 9.** Field 1 Observation B colour magnitude diagram (CMD): F172M versus F148W-F172M. The gray points are all detected sources in Observation B, the black points are the  $> 3\sigma$  variables, and the red points with error bars are the  $> 5\sigma$  variables. The error bars for the gray and black points are similar in size, but not shown to avoid crowding. Isochrones are from the CMD web isochrone generator at <http://stev.oapd.inaf.it/cmd>, and are plotted as the points joined by solid lines, with  $\log(\text{age})$  values of 6.6 (blue lines), 7.1 (magenta lines) and 7.6 (cyan lines).

counterpart search was carried out using the on-line tool Vizier (website <https://vizier.u-strasbg.fr/viz-bin/VizieR>, Ochsenbein et al. 2000). The UVIT positions are accurate to better than  $1''$  ( $1\sigma$  error of  $0.2''$ ) but the position accuracy of the counterparts is different for each catalog, typically  $\sim 1''$ , so we chose to use a search radius of  $2''$  within the UVIT position of each source. Several of the counterparts are extended sources (stellar clusters). Thus for those, the cluster effective radius,  $R_{\text{eff}}$ , is given in Table 4. The  $R_{\text{eff}}$  values range from 0.4 to  $2.5''$ . This was a factor in the choice of the  $2''$  search radius, because we did not want to miss stellar clusters within which the UVIT source resides.

The results are shown in Table 4, with counterpart position, type and distance in  $''$  from the UVIT position listed. One UVIT variable source had 3 counterparts, which are highly likely to be a single object with the reported positions differing by up to  $0.1''$ . 10 FUV variables had 2 listed counterparts, and the remainder had 1 counterpart. For the 10 cases with 2 counterparts (rows 2 to 11 in the table), most are likely the same object. The exceptions are row 2, where the globular cluster is not likely to be a counterpart, and row 9, where the two

objects are very different and we chose to put the planetary nebula first because of its much better position match. Some cases are ambiguous, e.g. for the sixth line in the table, the UVIT variable is within the cluster but because of the larger position offset may or may not be associated with the Wolf-Rayet star.

The following types of counterparts for the UVIT FUV variables were found. The main categories were: 9 matches with the Johnson et al. (2015) cluster catalog; 6 matches with ionized hydrogen (HII) regions; 6 matches with nova or nova candidates; 6 matches with unspecified variables and 5 matches with regular or semiregular variables. Smaller categories included: 2 hot supergiants and 1 S Doradus variable; 2 eclipsing binaries; 1 planetary nebula (PNe); 1 Cepheid; 1 Supernova Remnant (SNR) candidate; 1 unspecified transient and 1 foreground star in the Gaia DR2 catalog. One of the sources matching the cluster catalog also matched with a Wolf-Rayet star.

Overall, 42 of the 86 UVIT FUV  $> 5\sigma$  variables matched previously identified sources at other wavelengths. The clusters and HII regions are generally associated with young hot stars. Thus, most of the 42 identified sources are matched with a variable or match with a phenomenon associated with variability. The current results based on variability in FUV are therefore consistent with previous surveys.

The UVIT CMDs for the FUV  $> 5\sigma$  variables is shown in Figure 10 with Observation A data in the top panel and Observation B data in the bottom. The counterpart types are labelled using the First Catalog Match from Table 4. Not all 42 counterparts appear in both diagrams because a given counterpart may not have been measured in enough filters, or have a bright enough F148W, F172M or F179N in the given observation to show up on the CMD.

The brightest FUV variables, above the  $10^{7.1}$  year isochrone in both panels of Figure 10 are those identified as hot supergiants or residing in clusters, which is consistent with their locations in the CMDs. The S Dor star and the two hot supergiants have F148W magnitudes in Observations (A, B) of (18.24, 18.06), (17.83, 17.66) and (21.7, 22.9), respectively. Because the two brighter stars are so bright in FUV, the relatively small FUV variability of  $\sim 0.2$  magnitudes is significant at  $> 5\sigma$ . The FUV variables intermediate in luminosity, near the  $10^{7.1}$  year isochrone, are identified with some HII regions, other variables, and the Cepheid variable. The fainter FUV variables, near the  $10^{7.6}$  year isochrone, are identified with the eclipsing binaries, the remaining HII regions, regular or semiregular variables, one cluster and the PNe. The UVIT source identified with the cluster,

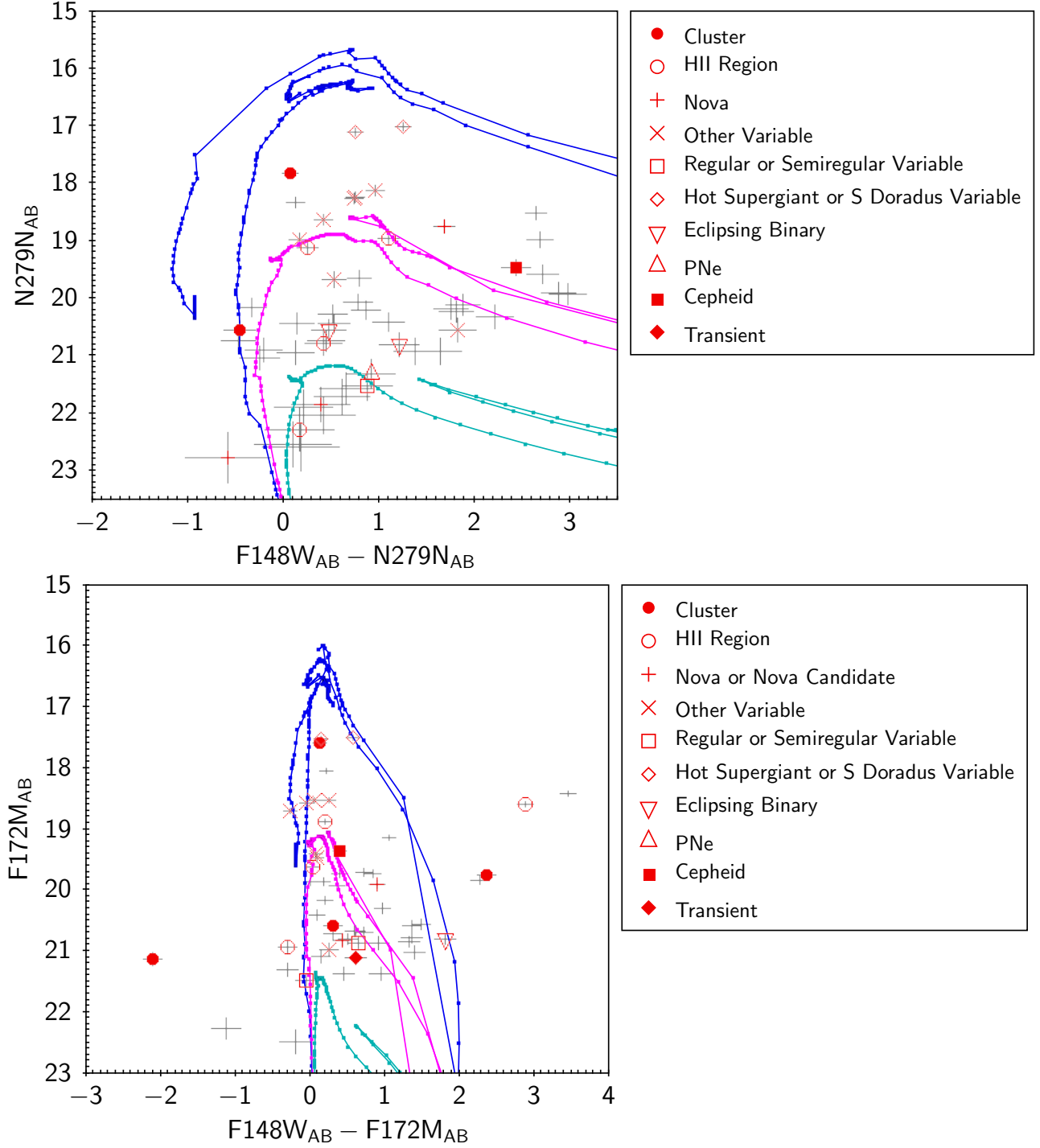


**Figure 10.** Top panel: Field 1 Observation A colour magnitude diagram (CMD) with  $N279N$  versus  $F148W-N279N$ . The gray points with error bars are the FUV  $> 5\sigma$  variable source measurements from Observation A, and the red symbols mark the identified counterparts from Table 4. Bottom panel: Field 1 Observation B colour magnitude diagram (CMD) with  $F172M$  versus  $F148W-F172M$ . In this case, the gray points with error bars are the FUV  $> 5\sigma$  variable source measurements from Observation B. Isochrones are from the CMD web isochrone generator at <http://stev.oapd.inaf.it/cmd>, and are plotted as the points joined by solid lines, with log(age) values of 6.6 (blue lines), 7.1 (magenta lines) and 7.6 (cyan lines).

Source No. 15 in Table 4, is the object that is the outlier in the lower panel of Figure 10 with F148W-F172M of  $-2.1$ . This UVIT source is at the edge of the cluster,  $1.86''$  from the cluster center, so may be an object with a bright UV flare unrelated to the cluster. The other object with a large change in color is Source No. 24, associated with a Cepheid variable. The F148W magnitude in changes from 21.89 in Observation A to 19.75 in Observation B.

Detailed modelling of the individual sources is beyond the scope of this work. The UVIT FUV variable source photometry catalog is published here to enable further investigation of individual sources. The full catalog is available online and a sample (the first 10 lines) of the catalog is given here in Table 2.

#### 4. SUMMARY AND CONCLUSION

Using a new observation of M31, Field 1 of the M31 UVIT survey now has been observed in FUV at two epochs separated by  $\simeq 3.1$  years. Field 1 is a 28 arcminute diameter (6.4 kpc) circular region centered on the M31 inner spiral arms and bulge. Using the source finding algorithm in CCDLAB, a list of source positions was constructed. These positions were then matched against the PHAT and Gaia DR2 catalogs. The analysis of differences in RA and in DEC and their standard deviation yields an astrometric accuracy of  $\sim 0.2''$  ( $1\sigma$ ) for the UVIT data. We carried out an analysis of the

photometry of extracted sources (details given in Appendix A), which allows for calibrated photometry in M31 in regions of moderate source crowding.

Field 1 in M31 includes a significant area around the bulge showing clear spiral arm structure (e.g. see images in Figures 1 and 2 of Leahy et al. 2018). The two epochs of Field 1 imaging in the UVIT F148W filter allows detection of variable FUV sources. A total 3164 sources were detected in both Observations A and B, 1383 were only detected in A, and 1431 were only detected in B. From this total of 5970 sources, 555 ( $\simeq 9\%$ ) were found to be variable by  $> 3\sigma$  and 86 ( $\simeq 1.5\%$ ) were found variable by  $> 5\sigma$ .

The mean FUV flux ratio from the two observations was found to be 3.1 for the 3 to 5  $\sigma$  variables, and 3.8 for the  $> 5\sigma$  variables. The magnitude distributions 3 to 5  $\sigma$  variables and  $> 5\sigma$  variables are flatter than for non-variables, well above the UVIT detection limit, giving evidence for a larger fraction of variables for the bright sources than for fainter sources. Analysis of the spatial distribution shows that a greater number of the variables are found in the spiral arms than between the spiral arms and that variables made up a greater percentage of the total number of sources in the spiral arms than outside the spiral arms. This is consistent with most variables being associated with young stellar systems concentrated in the spiral arms.

**Table 4.** Multiwavelength Counterparts of the UVIT FUV  $> 5\sigma$  Variables<sup>A</sup>.

Source No.	ra	dec	First catalog match	Distance	R <sub>eff</sub>	Second/third catalog match	Distance
1	10.8878	41.2029	S Doradus variable <sup>1</sup>	0.18		Luminous blue variable <sup>13</sup>	0.02
2	10.9133	41.1721	Hot supergiant variable <sup>2</sup>	0.85		No coherent periodicity to variability <sup>15</sup>	0.06
3	10.7224	41.4502	Hot supergiant variable <sup>2</sup>	0.32		Globular cluster <sup>14,19</sup>	0.69
4	10.8951	41.1651	Cluster <sup>3</sup>	1.223	2.56	Dubious variable <sup>15</sup>	0.17
5	10.9456	41.2100	Variable <sup>4</sup>	1.092		Variable <sup>16</sup>	0.697
6	10.9462	41.2107	Cluster <sup>3</sup>	0.941	2.30	Ionized nebulae <sup>17</sup>	0.748
7	10.8020	41.3939	Eclipsing binary <sup>5</sup>	0.08		Wolf Rayet star <sup>18</sup>	1.14
8	10.8152	41.1498	Nova <sup>1</sup>	0.35		Variable <sup>4</sup>	0.761
9	10.6131	41.2485	Planetary nebula <sup>6</sup>	0.25		Variable <sup>4</sup>	0.286
10	10.7564	41.2358	Regular or semi regular variable <sup>7</sup>	1.589		Regular or semi regular variable <sup>7</sup>	1.344
11	10.5834	41.2227	Regular or semi regular variable <sup>7</sup>	1.887		Variable <sup>4</sup>	1.175
12	10.8734	41.3117	Cluster <sup>3</sup>	0.104	0.64	Variable <sup>4</sup>	1.526
13	10.9463	41.2010	Variable <sup>4</sup>	1.305			
14	10.7236	41.4499	Cluster <sup>3</sup>	1.001	2.08		
15	10.7231	41.4494	Cluster <sup>3</sup>	1.86	2.08		
16	10.8837	41.1705	Variable <sup>4</sup>	1.517			
17	10.8715	41.3116	Variable <sup>4</sup>	0.656			
18	10.8654	41.3066	Cluster <sup>3</sup>	0.335	0.41		
19	10.9478	41.1987	HII region <sup>8</sup>	1.50			
20	10.9972	41.2927	HII region <sup>8</sup>	0.20			
21	10.9340	41.4046	Variable <sup>4</sup>	0.643			
22	10.5480	41.2676	Regular or semi regular variable <sup>7</sup>	0.844			
23	10.8645	41.2649	HII region <sup>8</sup>	0.40			
24	10.9929	41.2960	Cepheid variable <sup>9</sup>	1.613			
25	10.6581	41.2338	Regular or semi regular variable <sup>7</sup>	0.386			
26	10.9331	41.1952	Foreground source <sup>10</sup>	1.373			
27	10.9191	41.4306	Cluster <sup>3</sup>	0.247	0.44		
28	10.7521	41.2013	Regular or semi regular variable <sup>7</sup>	1.656			
29	10.9933	41.2283	Cluster <sup>3</sup>	0.079	0.88		
30	10.9255	41.4311	Cluster <sup>3</sup>	0.269	0.49		
31	10.9418	41.4034	Eclipsing binary <sup>5</sup>	0.23			
32	10.9959	41.2458	Variable <sup>11</sup>	0.59			
33	10.9879	41.1993	HII region <sup>8</sup>	0.33			
34	10.8643	41.3113	HII region <sup>8</sup>	1.08			
35	10.4871	41.1909	Nova <sup>12</sup>	0.92			
36	10.8137	41.3379	Nova Candidate <sup>20</sup>	0.68			
37	10.9535	41.4080	HII region <sup>8</sup>	1.73			

*Table 4 continued*

Table 4 (*continued*)

Source No.	ra	dec	First catalog match	Distance	R <sub>eff</sub>	Second/third catalog match	Distance
38	10.5813	41.1871	Supernova Candidate <sup>21</sup>	0.03			
39	10.7564	41.2999	Nova <sup>22</sup>	0.24			
40	10.7536	41.3218	Nova <sup>23</sup>	1.11			
41	10.6379	41.2191	Nova Candidate <sup>24</sup>	0.10			
42	10.5981	41.1979	Transient event <sup>25</sup>	0.22			

NOTE—A: ra and dec are sky position of the UVIT FUV variable in decimal degrees; first, second, and third catalog matches refer to the identified typing of the object in catalogs in Vizier; distance refers to the separation in arcseconds between the UVIT source and the identified match from Vizier. R<sub>eff</sub> gives the radius of the cluster from the literature for sources that match with a cluster.

Catalog references: 1. Samus' et al. (2017), 2. Humphreys et al. (2017b), 3. Johnson et al. (2015), 4. An et al. (2004), 5. Vilardell et al. (2006), 6. Halliday et al. (2006), 7. Fliri et al. (2006), 8. Azimlu et al. (2011), 9. Kodric et al. (2018), 10. Gaia Collaboration (2018), 11. Kurtev (2003), 12. Hornoch & Kucakova (2016a), 13. Humphreys et al. (2017a), 14. Kim et al. (2007), 15. Heinze et al. (2018), 16. Bonanos et al. (2019), 17. Walterbos & Braun (1994), 18. Neugent et al. (2012), 19. Peacock et al. (2010), 20. Williams & Darnley (2015), 21. Hornoch & Kucakova (2016b), 22. Hornoch & Kucakova (2019a), 23. Hornoch & Kucakova (2019b), 24. Ovcharov et al. (2015), 25. Soraisam et al. (2019).



CMDs for Observation A and for Observation B show that most sources detected in FUV are consistent with relatively young stellar populations. The range of inferred age for the variables is  $\sim 5 \times 10^6$  yr to  $\sim 1 \times 10^8$  yr. The variable stars, in comparison to the non-variable stars are concentrated at younger ages, confirming that most variable stars are associated with younger stellar populations. This is consistent with the results from the spatial analysis.

The  $> 5\sigma$  variables were position-matched to catalogs of known sources. Of the 86 sources, 42 had a match to a previously known source. Most of these were with known variable sources. The main categories include star clusters, HII regions, nova or nova candidates, regular or semiregular variables, other variables, and hot supergiants. This confirms that UVIT FUV measurements can select hot variable stars as well as other types of FUV variables such as novae.

A catalog of the UVIT photometry of the variables is presented, and is available on-line with this paper. The

aim is to facilitate future multiwavelength research of individual objects of interest.

This work is supported by funding from the Canadian Space Agency. This publication uses data from the AstroSat mission of the Indian Space Research Institute (ISRO), archived at the Indian Space Science Data Center (ISSDC). This work has made use of data from the European Space Agency (ESA) mission *Gaia* (<https://www.cosmos.esa.int/gaia>), processed by the *Gaia* Data Processing and Analysis Consortium (DPAC, <https://www.cosmos.esa.int/web/gaia/dpac/consortium>). Funding for the DPAC has been provided by national institutions, in particular the institutions participating in the *Gaia* Multilateral Agreement. We thank the anonymous referee for comments which lead to several improvements in this article.

## APPENDIX

### A. TESTS TO DETERMINE SOURCE EXTRACTION FOR CROWDED FIELDS

The images we used were created using CCDLAB, including various corrections such as pointing drift correction, flat field correction and astrometry calibration. For one of the first tests, we compared source fitting on the CCDLAB image with source fitting on the image after smoothing. Convolution of the image with Gaussians of various FWHM were tried, and we found that a the image smoothed with 1.5 pixel FWHM Gaussian worked well as a compromise between producing better fits and not compromising spatial resolution. This 1.5 pixel convolution is termed the smoothed image. The smoothed image resulted in better fits to point sources than the unsmoothed image, mainly because of a much smaller fraction of bad fits (fits which failed to produce reasonable fits to the image). As an example, the brightest 100 sources in N279N Field 2 were fit using smoothed and unsmoothed images. The mean least-squares of the fits for the smoothed image was much smaller (2.6 vs. 6250 for the unsmoothed image). Because of these tests, the resultant convolution was applied to all of the images before fitting.

The HST-PHAT survey has accurate positions and photometry in the NUV F275W filter (275nm band), which we could use to calibrate the UVIT observations. We used M31 Fields 1, 2, 7 and 13 for developing the source extraction method because they had N279N 280 nm band observations that overlap with HST-PHAT observations. Field 2 was the main test field because it had the largest overlap with the HST-PHAT survey.

For Fields with N279N, 7x7 pixel circular and elliptical Gaussian and Moffat functions were fit to 15 bright, isolated sources for each filter. Similarly, Curves of Growth (COGs) with a half-width of 26 pixels were fit to each of these sources. A linear regression line was fit to the COG fluxes vs Gaussian or Moffat fluxes for the 15 sources for each filter. The fits gave conversion factors from flux for each of the other fitting types to the COG flux. The resulting factors and their standard deviations are shown in Table 5.

**Table 5.** Conversion factors between 7x7 Circular and Elliptical Gaussian and Moffat fits and a COG with radius 26 for 15 bright sources in Field 2.

	Conversion Factor
Gaussian, Circular	1.617 $\pm$ 0.044
Gaussian, Elliptical	1.580 $\pm$ 0.037
Moffat, Circular	0.460 $\pm$ 0.716
Moffat, Elliptical	0.386 $\pm$ 0.396

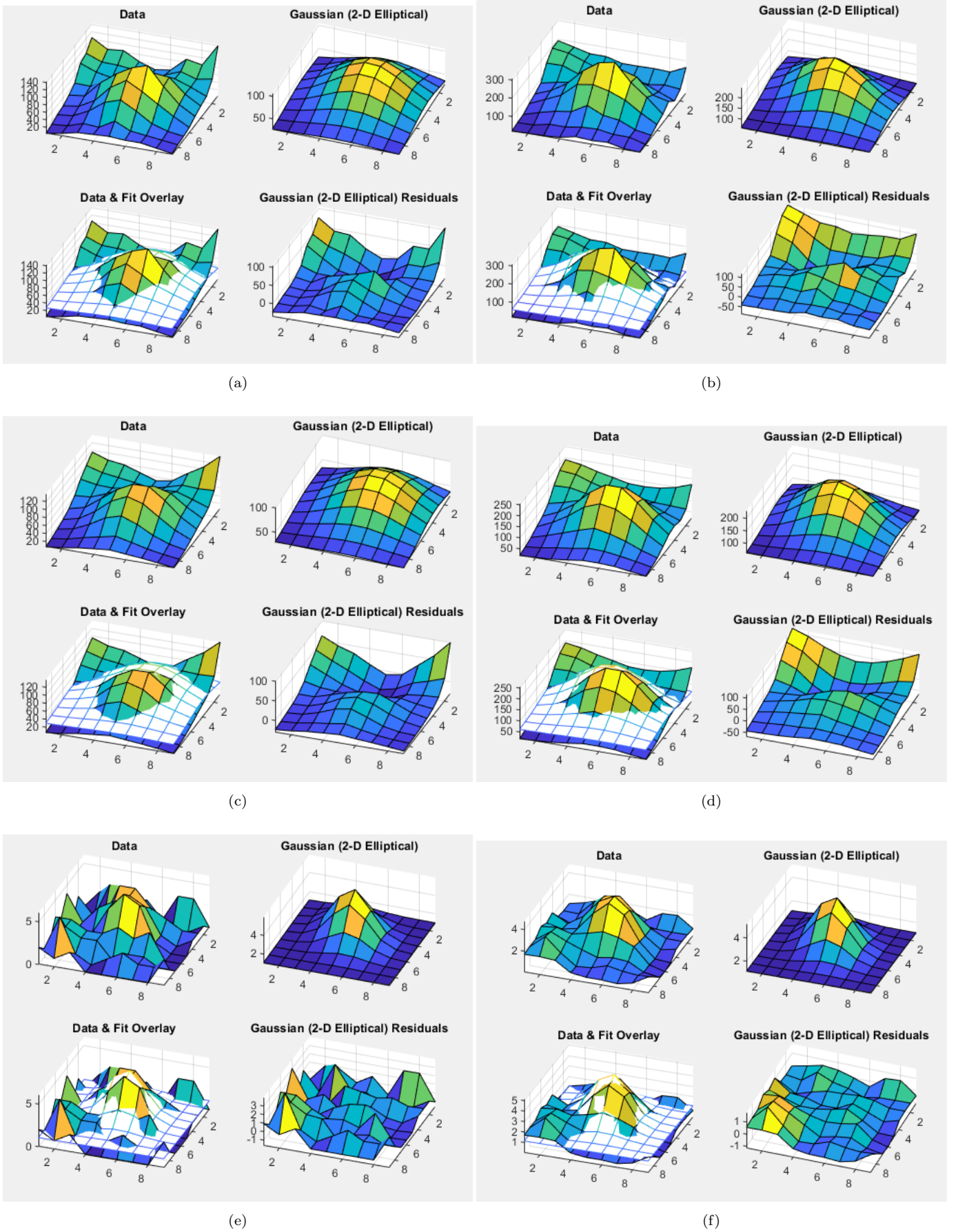


**Figure 11.** Plot of Elliptical Gaussian fits to selected variable sources, showing data, model, data and model overlay, and residuals for each fit: (a) Source N1 observation A (no smoothing); (b) Source N1 observation B (no smoothing); (c) Source N1 observation A (smoothed); (d) Source N1 observation B (smoothed); (e) Source SWbulge1 observation A (no smoothing); (f) Source SWbulge1 observation A (smoothed); (see text for details).

We examined the regression fits to determine which fitting type best fits a large number of sources with a small box size. The Moffat fits were frequently skewed by low volume sources, which it over-fit with unrealistic numbers. On the other hand, the Gaussian fits were found to be proportional to the COG with a small standard deviation. Since the elliptical Gaussian fits have the least variance when compared to the COG, this was chosen as the best fitting function to determine volumes.

To determine the best sized fitting box to use, 7x7 and 9x9 elliptical Gaussian fits were then performed on the N279N Field 2 image and compared with the F275W filter photometry from PHAT. We also tried 5x5 but that resulted in many poor fits and incorrect photometry, and 11x11 but it had too many regions affected by adjacent sources. The ratios in source counts from the Gaussian fit with 7x7 and 9x9 boxes to counts from the COG were found. The scatter (standard deviation) in the ratios was significantly larger for the 7x7 fits than for the 9x9 fits. Thus 9x9 was chosen as the better size. Figure 11 illustrates fits for an average-brightness source (top 4 panels) and a faint source (lower 2 panels) from the F148W  $> 5\sigma$  variable source list. Each panel shows data (upper-left sub-plot), fit (upper right subplot), overlay (lower-left subplot) and residuals (lower-right subplot). The top row (a and b) shows the fits for a source, labelled N1, in the northern part of the field shown in Figure 2, comparing the A (left) and B (right) source fits on the unsmoothed images. The middle row (c and d) shows the fits for N1 on the smoothed A and B images. The residuals are significantly lower for the smoothed images. This source has nearby sources at 2 of the 4 corners of the 9x9 region, thus it would be impossible to use COG photometry on it. The bottom row (e and f) shows the fits for a faint source southwest of the bulge (southwest of the blank area in Figure 2), labelled SWbulge1, comparing the unsmoothed A (left) and smoothed A (right) fits. The SWbulge source is faint and in a crowded region of high background, with probable fainter sources at 3 of the 4 corners of the 9x9 fit region. For this source the difference in residuals between smoothed and unsmoothed fits is apparent.

To find the best constraints for the sources, the 100 brightest PHAT sources were fit with elliptical Gaussians in CCDLAB and the range of parameters was constrained to the smallest and largest reasonable values. Outliers (fits that failed to converge) included a few sources with sigmas less than 0.6 pixels and some with sigmas greater than 4 pixels. Ignoring these, the sigmas of the fitted elliptical Gaussians ranged from 1.1 to 2.2 pixels, so these were chosen as constraints for the sources. Using the constraints, the least-squares of the fits was much lower than without the constraints.

Using the smoothed N279N Field 2 image, constrained 9x9 elliptical Gaussians were fit and compared with COGs of half width 12, 14, 17, 20 and 25. At a width of 25, nearby sources were visible at the edge of the fit, so this was the largest COG used. For the other Fields and filters there were not enough isolated sources unless we used only the COG half widths of 12, 14 and 17. The COGs at each of these radii correspond well with the trend observed in Tandon et al. (2020). Thus, a first conversion factor was found from the 9x9 elliptical Gaussian to each of the 12, 14, and 17 half-width COGs, and a second conversion factor from these smaller COGs to a 95 pixel COG using the table from Tandon et al. (2020). An overall conversion factor was then obtained from combining the two conversion factors for COG half-width, then averaging the values from the different COG half-widths. This was carried out for each filter. A list of factors for the different Fields and filters is shown in Table 6.

**Table 6.** Gaussian to COG Conversion factors for M31 Fields 1, 2, 7, and 13 in UVIT.

Field	F148W	F172M	F169M	N279N	N219M
1	$1.529 \pm 0.093$	$1.653 \pm 0.014$	$1.542 \pm 0.017$	$1.654 \pm 0.020$	$1.621 \pm 0.025$
2	$1.694 \pm 0.027$	$1.650 \pm 0.043$	N/A	$1.646 \pm 0.009$	$1.646 \pm 0.028$
7	$1.606 \pm 0.035$	$1.647 \pm 0.017$	N/A	$1.784 \pm 0.012$	$1.942 \pm 0.020$
13	$1.671 \pm 0.016$	$1.582 \pm 0.008$	N/A	$1.719 \pm 0.021$	$1.820 \pm 0.019$

Using the trapezoidal integral function in numpy in python (numpy.trapz), the Vega flux and standard AB flux were integrated over the N279N filter profile. From this, the difference in magnitude between the two measurement systems was found to be 1.483. This allows for comparison between the PHAT and UVIT magnitudes (Williams et al. 2014).

The corrected magnitude in N279N was compared against the F275W PHAT magnitudes for sources brighter than AB magnitude 22 in UVIT and brighter than Vega magnitude 20.5 in PHAT. The two were fit with the python function scipy.optimize.curve\_fit to determine the difference in intercept between the two. From this, a difference of  $1.613 \pm 0.013$  was obtained. As such, an additional correction factor of 0.130 was applied to the magnitudes, which corresponds to

the difference between the measured and expected difference between UVIT and PHAT. These correction factors are given in Table 7.

**Table 7.** Correction for N279N in UVIT based on F275W in PHAT.

Field	Correction (magnitudes)
1	$0.105 \pm 0.021$
2	$0.130 \pm 0.013$
7	$0.168 \pm 0.013$
13	$0.075 \pm 0.031$

## REFERENCES

- An, J. H., Evans, N. W., Hewett, P., et al. 2004, VizieR Online Data Catalog, J/MNRAS/351/1071
- Astropy Collaboration, Robitaille, T. P., Tollerud, E. J., et al. 2013, A&A, 558, A33
- Azimlu, M., Marciniak, R., & Barmby, P. 2011, AJ, 142, 139,
- Bertin, E., & Arnouts, S. 1996, A&AS, 117, 393
- Bonanos, A. Z., Yang, M., Sokolovsky, K. V., et al. 2019, VizieR Online Data Catalog, J/A+A/630/A92
- Corrales, L. 2015, ApJ, 805, 23
- Ferland, G. J., Porter, R. L., van Hoof, P. A. M., et al. 2013, RMxAA, 49, 137
- Fliri, J., Riffeser, A., Seitz, S., & Bender, R. 2006, VizieR Online Data Catalog, J/A+A/445/423
- Gaia Collaboration, Prusti, T., de Bruijne, J. H. J., et al. 2016, A&A, 595, A1. doi:10.1051/0004-6361/201629272
- Gaia Collaboration, Brown, A. G. A., Vallenari, A., et al. 2018, A&A, 616, A1. doi:10.1051/0004-6361/201833051
- Gaia Collaboration. 2018, VizieR Online Data Catalog, I/345
- Halliday, C., Carter, D., Bridges, T. J., et al. 2006, VizieR Online Data Catalog, J/MNRAS/369/97
- Hanisch, R. J., & Biemesderfer, C. D. 1989, BAAS, 21, 780
- Heinze, A. N., Tonry, J. L., Denneau, L., et al. 2018, AJ, 156, 241
- Hornoch, K., & Kucakova, H. 2016a, The Astronomer’s Telegram, 9373, 1
- . 2016b, The Astronomer’s Telegram, 8785, 1
- . 2019a, The Astronomer’s Telegram, 13207, 1
- . 2019b, The Astronomer’s Telegram, 12925, 1
- Humphreys, R. M., Davidson, K., Hahn, D., Martin, J. C., & Weis, K. 2017a, VizieR Online Data Catalog, J/ApJ/844/40
- Humphreys, R. M., Gordon, M. S., Martin, J. C., Weis, K., & Hahn, D. 2017b, VizieR Online Data Catalog, J/ApJ/836/64
- Johnson, L. C., Seth, A. C., Dalcanton, J. J., et al. 2015, ApJ, 802, 127
- Kim, S. C., Lee, M. G., Park, H. S., et al. 2007, in Astronomical Society of the Pacific Conference Series, Vol. 362, The Seventh Pacific Rim Conference on Stellar Astrophysics, ed. Y. W. Kang, H. W. Lee, K. C. Leung, & K. S. Cheng, 286
- Kodric, M., Riffeser, A., Hopp, U., et al. 2018, VizieR Online Data Catalog, J/AJ/156/130
- Kurtev, R. G. 2003, Astronomische Nachrichten, 324, 265
- Leahy, D. A., Bianchi, L., & Postma, J. E. 2018, AJ, 156, 269
- Leahy, D. A., Postma, J., Chen, Y., et al. 2020, ApJS, 247, 47. doi:10.3847/1538-4365/ab77a9
- Leahy, D. A. & Chen, Y. 2020, ApJS, 250, 23
- Leahy, D. A., Postma, J., Buick, M., et al. 2020, arXiv:2012.02727
- Martin, D. C., Fanson, J., Schiminovich, D., et al. 2005, ApJL, 619, L1. doi:10.1086/426387
- McConnachie, A. W., Irwin, M. J., Ferguson, A. M. N., et al. 2005, MNRAS, 356, 979. doi:10.1111/j.1365-2966.2004.08514.x
- Neugent, K. F., Massey, P., & Georgy, C. 2012, ApJ, 759, 11
- Lamport, L. 1994, LaTeX: A Document Preparation System, 2nd Edition (Boston, Addison-Wesley Professional)
- Ochsenbein, F., Bauer, P., & Marcout, J. 2000, A&AS, 143, 23. doi:10.1051/aas:2000169
- Ovcharov, E., Kostov, A., Kurtenkov, A., Valcheva, A., & Nedialkov, P. 2015, The Astronomer’s Telegram, 7065, 1
- Peacock, M. B., Maccarone, T. J., Knigge, C., et al. 2010, VizieR Online Data Catalog, J/MNRAS/402/803
- Postma, J. E. & Leahy, D. 2017, PASP, 129, 115002. doi:10.1088/1538-3873/aa8800

- Postma, J. E. & Leahy, D. 2020, PASP, 132, 054503.  
doi:10.1088/1538-3873/ab7ee8
- Samus', N. N., Kazarovets, E. V., Durlevich, O. V.,  
Kireeva, N. N., & Pastukhova, E. N. 2017, Astronomy  
Reports, 61, 80
- Schwarz, G. J., Ness, J.-U., Osborne, J. P., et al. 2011,  
ApJS, 197, 31
- Vogt, F. P. A., Dopita, M. A., Kewley, L. J., et al. 2014,  
ApJ, 793, 127
- Singh, K. P., Tandon, S. N., Agrawal, P. C., et al. 2014,  
Proc. SPIE, 9144, 91441S. doi:10.1117/12.2062667
- Soraisam, M., Lee, C.-H., Narayan, G., Matheson, T., &  
Saha, A. 2019, The Astronomer's Telegram, 13210, 1
- Tandon, S. N., Subramaniam, A., Girish, V., et al. 2017,  
AJ, 154, 128
- Tandon, S. N., Postma, J., Joseph, P., et al. 2020, AJ, 159,  
158
- Taylor, M. B. 2005, in Astronomical Society of the Pacific  
Conference Series, Vol. 347, Astronomical Data Analysis  
Software and Systems XIV, ed. P. Shopbell, M. Britton,  
& R. Ebert, 29
- Vilardell, F., Ribas, I., & Jordi, C. 2006, VizieR Online  
Data Catalog, J/A+A/459/321
- Walterbos, R. A. M., & Braun, R. 1994, VizieR Online  
Data Catalog, J/A+AS/92/625
- Williams, B. F., Lang, D., Dalcanton, J. J., et al. 2014,  
ApJS, 215, 9
- Williams, S. C., & Darnley, M. J. 2015, The Astronomer's  
Telegram, 8218, 1